




RESEARCH ARTICLE | AUGUST 01 2023

Band gap energy and near infrared to ultraviolet complex optical properties of single crystal $TbScO_3$ FREE

Emily Amonette ; Prabin Dulal ; Dylan Sotir ; Matthew Barone ; Darrell Schlom ; Nikolas J. Podraza 

 Check for updates

Appl. Phys. Lett. 123, 052103 (2023)

<https://doi.org/10.1063/5.0146670>




View Online




Export Citation


25 August 2024 15:40:49




Nanotechnology & Materials Science




Optics & Photonics



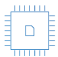
Impedance Analysis




Scanning Probe Microscopy



Sensors




Failure Analysis & Semiconductors



Unlock the Full Spectrum.
From DC to 8.5 GHz.

Your Application. Measured.

Find out more



Band gap energy and near infrared to ultraviolet complex optical properties of single crystal TbScO₃

Cite as: Appl. Phys. Lett. **123**, 052103 (2023); doi: [10.1063/5.0146670](https://doi.org/10.1063/5.0146670)

Submitted: 15 February 2023 · Accepted: 20 July 2023 ·

Published Online: 1 August 2023



View Online



Export Citation



CrossMark

Emily Amonette,^{1,2,a)} Prabin Dulal,^{1,2} Dylan Sotir,³ Matthew Barone,³ Darrell Schlom,³ and Nikolas J. Podraza^{1,2}

AFFILIATIONS

¹Department of Physics and Astronomy, University of Toledo, Toledo, Ohio 43606, USA

²Wright Center for Photovoltaics Innovation and Commercialization, University of Toledo, Toledo, Ohio 43606, USA

³Department of Materials Science and Engineering, Cornell University, Ithaca, New York 14850, USA

^{a)} Author to whom correspondence should be addressed: emily.miller12@rockets.utoledo.edu

ABSTRACT

TbScO₃ is a wide bandgap semiconductor with potential applications in charge trap memory devices and acts as an alternate gate dielectric in fully depleted transistors and also a substrate for epitaxial thin film growth. TbScO₃ has an orthorhombic crystal structure, which gives rise to optical anisotropy. Generalized ellipsometric spectra are measured for multiple in-plane rotations of (110) and (001) oriented TbScO₃ single crystals over a photon energy range of 0.7–8.5 eV to determine the complex dielectric function ($\epsilon = \epsilon_1 + i\epsilon_2$) spectra for electric fields oscillating along each axis. A direct bandgap is identified at 6.50 eV, and above gap critical point transitions are found at 6.99, 7.14, 7.16, 7.21, and 7.42 eV.

Published under an exclusive license by AIP Publishing. <https://doi.org/10.1063/5.0146670>

Terbium scandate (TbScO₃) has potential for applications and acts as a high-k dielectric in charge trap memory devices,¹ an alternative gate dielectric in fully depleted transistors,² and as a substrate for epitaxial thin film growth.³ Single crystal TbScO₃ at room temperature has an orthorhombic crystal structure belonging to the space group Pnma with lattice parameters $a = 5.4543$, $b = 5.7233$, and $c = 7.9147$ Å.⁴ Band gap values for TbScO₃ have been previously reported from 5.4 to 6.1 eV.^{5–7} Due to its structural anisotropy, electric fields oscillating parallel to each crystallographic axis experience a different response, resulting in optical anisotropy. The (110) crystal orientation yields sensitivity to the optic response perpendicular and parallel to the c-axis but does not enable distinction between that of the a- and b-axes. The (001) crystal orientation adds sensitivity to the separate a- and b-axes with the directions of the a- and b-axes confirmed by x-ray diffraction measurements.

In this work, the near infrared to vacuum ultraviolet anisotropic complex optical properties of TbScO₃ are determined from generalized ellipsometric measurements over a photon energy range from 0.7 to 8.5 eV. Two commercially available Czochralski grown TbScO₃ single crystals are measured. One has been cut to expose the (110) surface plane so that the c-axis lies parallel to that surface (MTI Corp.), and the other has been cut to expose the (001) surface plane so that the a- and b-axes lie parallel to the surface (SurfaceNet). A divided spectral

range analysis approach of measured generalized ellipsometric spectra is used to determine the complex dielectric function ($\epsilon = \epsilon_1 + i\epsilon_2$) spectra in each of the three crystallographic directions.^{8–10} The direct bandgap energy is identified at 6.50 ± 0.04 eV, and above gap critical points are found at 6.99 ± 0.09 , 7.14 ± 0.02 , 7.16 ± 0.01 , 7.21 ± 0.03 , and 7.42 ± 0.46 eV.

A vacuum ultraviolet ellipsometer¹¹ (J.A. Woollam Co., Inc. VUV-VASE) is used to measure generalized ellipsometric spectra at a 70° angle of incidence over a spectral range from 0.7 to 8.5 eV on both crystals as received from the manufacturers. A single angle of incidence is sufficient to sample electric fields oscillating parallel to each of the three crystallographic axes as both (110) and (001) oriented TbScO₃ crystals are characterized.^{12,31} Spectra between 3.0 and 4.0 eV have been omitted due to excessive noise caused by low sample reflectance in this range. Since the material is anisotropic, the measured ellipsometric spectra vary with crystal orientation or rotation about an axis normal to the sample surface plane. Three generalized ellipsometry measurements are taken with the samples rotated about an axis normal to their surface planes to determine the unique azimuthal Euler angle (ϕ) for each measurement. Initial analysis of each crystal cut is performed separately. The polar Euler angle (θ) is invariant with these sample rotations and fixed at 90° and 0° for the (110) and (001) samples, respectively, due to their crystal orientations. The Euler angle

ψ is fixed at 0 degrees for the (001) cut crystal, while ψ is arbitrary for the (110) cut crystal as it is treated as uniaxial during divided spectral range analysis. The (110) cut can be treated as uniaxial because neither the a- nor the b-axis lies parallel to the sample surface plane, with the a-axis making an angle of $\sim 46^\circ$ with respect to the surface and the b-axis making an angle of $\sim 44^\circ$. Electric field components perpendicular to the c-axis but parallel to the surface plane will sample a convolution of the optical response along the a- and b-axes regardless of angle of incidence, so the measurement of the (110) cut crystal does not have sensitivity to these individual axes, only a convolution of the two. The three sample rotations between measurements leading to variations in ϕ provide further sensitivity to the optical response parallel to the c-axis as well as the convolution of the a- and b-axes optical response perpendicular to the c-axis but parallel to the (110) surface plane. Similarly, the three sample rotations of the (001) cut crystal yield sensitivity to the a- and b-axes as those axes lie in the sample surface plane, but there is little sensitivity to the c-axis as it is perpendicular to the sample surface, and its optical response has been fixed to that obtained from the analysis of the (110) cut crystal. By analyzing each crystal cut separately, the resulting divided spectral range models provide the structural parameters of surface layer thicknesses for each crystal and ϕ for each measurement rotation in order to account for the optical response of all three crystallographic axes. These models serve as starting points for numerical inversion, which determines spectra in ε from 0.7 to 8.5 eV for the three crystallographic directions. Figure S-7 in the supplementary material outlines the analysis procedure.

Experimental data are fitted using least squares regression analysis with an unweighted error function σ , which is defined in generalized N_{xy} ($=\cos 2\psi_{xy}$), C_{xy} ($=\sin 2\psi_{xy}\cos \Delta_{xy}$), and S_{xy} ($=\sin 2\psi_{xy}\sin \Delta_{xy}$), where $(x = p, s; y = p, s)$ notation as

$$\sigma = \left\{ \frac{1}{3n - m} \sum_{i=1}^n \left[\left(N_{pp,i}^{\text{mod}} - N_{pp,i}^{\text{exp}} \right)^2 + \left(C_{pp,i}^{\text{mod}} - C_{pp,i}^{\text{exp}} \right)^2 + \left(S_{pp,i}^{\text{mod}} - S_{pp,i}^{\text{exp}} \right)^2 + \left(N_{ps,i}^{\text{mod}} - N_{ps,i}^{\text{exp}} \right)^2 + \left(C_{ps,i}^{\text{mod}} - C_{ps,i}^{\text{exp}} \right)^2 + \left(S_{ps,i}^{\text{mod}} - S_{ps,i}^{\text{exp}} \right)^2 + \left(N_{sp,i}^{\text{mod}} - N_{sp,i}^{\text{exp}} \right)^2 + \left(C_{sp,i}^{\text{mod}} - C_{sp,i}^{\text{exp}} \right)^2 + \left(S_{sp,i}^{\text{mod}} - S_{sp,i}^{\text{exp}} \right)^2 \right] \right\}^{1/2}, \quad (1)$$

where n is the number of measured data points and m is the number of variable model parameters.^{13,14} The superscripts “exp” and “mod” refer to experimentally measured and model-simulated data, respectively. The subscripts “pp,” “ps,” and “sp” refer to N , C , and S corresponding to $\rho_{pp} = \bar{r}_{pp}/\bar{r}_{ss}$, $\rho_{ps} = \bar{r}_{ps}/\bar{r}_{pp}$, and $\rho_{sp} = \bar{r}_{sp}/\bar{r}_{ss}$, respectively.¹⁵ The unweighted error function is chosen because reported error for the equipment in terms of N , C , and S is 0.001 with no spectral dependence assumed. Experimental data and model fits are shown in the supplementary material.

Divided spectral range analysis is applied by using separate physically realistic parametric models to describe ε in the transparent spectral range from 0.7 to 5 eV and the highly absorbing spectral range from 7 to 8.5 eV, while the structural parameters are kept common for each respective sample. The weakly absorbing region, in this case between 5 and 7 eV, is ignored as to not generate a bias in the obtained parameters due to the assumption of a particular model for ε in the

vicinity of the bandgap, as has been previously demonstrated.^{8–10,19} The structural model consists of the anisotropic biaxial semi-infinite TbScO₃ substrate and an anisotropic biaxial surface layer resulting in a common surface thickness for all measurements of each sample and unique ϕ for each measurement. The spectra in ε of the surface layer are described by a Bruggeman effective medium approximation (EMA).¹⁷ In the anisotropic case, the Bruggeman EMA treats the surface as a second anisotropic layer with identical Euler angles as the bulk crystal in the fitting analysis. The complex dielectric function spectra of the EMA in each crystallographic direction are represented by equal parts void and the corresponding bulk material along that crystal axis. The EMA layer describes a lower optical density portion of the material that is different from the bulk, including surface roughness and other surface effects such as hydrocarbons from atmospheric exposure. The surface layers are determined to have thicknesses of 8.7 ± 2.4 nm for the (001) sample and a 12.6 ± 0.5 nm for the (110) sample. Atomic force microscopy (AFM) yields comparable root mean square thicknesses of 2.91 and 8.30 nm for the (001) and (110) oriented samples. The values of these two characterization techniques are comparable to one another, as spectroscopic ellipsometry commonly overestimates the thickness of surface layers compared to AFM^{17,18} as AFM provides a surface profile, while spectroscopic ellipsometry is sensitive to a region of different optical responses than the bulk which may include the aforementioned surface affects as well as lower subsurface density.

Spectra in ε in the transparent region are described by a Sellmeier expression¹⁹

$$\varepsilon(E) = \varepsilon_\infty + \frac{2}{\pi} \left(\frac{AE_0}{E_0^2 - E^2} \right), \quad (2)$$

where A is the amplitude, E_0 is the resonance energy, and ε_∞ is a constant additive term. In the highly absorbing region, spectra in ε are parameterized using Sellmeier terms and a sum of critical point parabolic band (CPPB) oscillators²⁰ each described by

$$\varepsilon_{\text{CPPB}}(E) = A_n e^{i\phi_n} \left(\frac{\Gamma_n}{2E_n - 2E - i\Gamma_n} \right)^{\mu_n}, \quad (3)$$

where A_n is the amplitude, E_n is the critical point resonance energy, Γ_n is the critical point broadening, ϕ_n is the phase projection factor, and μ_n is the dimensionality of the critical point. Allowed dimensionality values are -0.5 , 0 , 0.5 , and 1 , which correspond to three dimensional, two dimensional, one dimensional, and excitonic transitions, respectively. Values for the Euler angle ϕ are shown in Table I. Divided spectral range model fits are shown in Figs. S-1 and S-2. After completing divided spectral range analysis, surface thickness and ϕ are fixed for each measurement, and a Kramers–Kronig consistent B-spline is used

TABLE I. Azimuthal Euler angle ϕ parameters from divided spectral range analysis for (110) and (001) crystal cuts.

(110) ϕ ($^\circ$)	(001) ϕ ($^\circ$)
66.9 ± 10.7	44.1 ± 17.5
150.6 ± 27.7	81.9 ± 6.7
-83.5 ± 4.4	133.2 ± 17.8

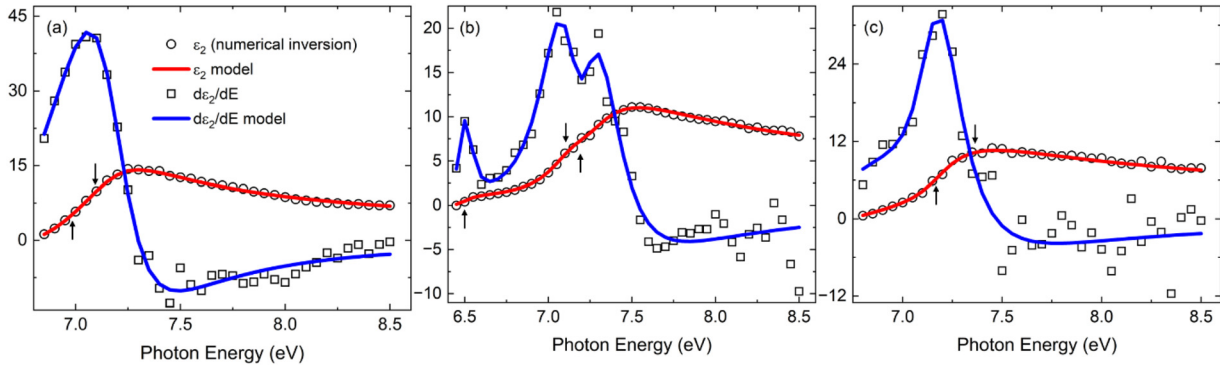


FIG. 1. Spectra in ϵ_2 of TbScO₃ obtained by numerical inversion (symbols) and parameterization of ϵ_2 (red lines) simultaneously with its derivative (blue lines) using critical point parabolic band (CPPB) oscillators in directions parallel to the (a) a-, (b) b-, and (c) c-axes. Arrows indicate critical point energies.

to approximate ϵ over the entire spectral range, including the weakly absorbing region, without a bias to a particular optical property line shape. The B-spline representation of ϵ also generates Kramers–Kronig consistent starting values for subsequent numerical inversion¹⁶ to determine ϵ parallel to each crystal axis over the full measured spectral range. Numerical inversion is first performed on the three sets of data from the (110) oriented crystal cut in order to obtain reliable spectra in ϵ parallel to the c-axis and then on the three sets of data for the (001) oriented crystal cut in order to obtain spectra in ϵ parallel to the a- and b-axes. Numerical inversion fits are shown in Figs. S-3 and S-4.

The σ values for the numerical inversion spectra as seen in Figs. S-3 and S-4 are 6.45×10^{-2} and 6.43×10^{-2} for the (001) and (110) crystal cuts, respectively. These values indicate a good quality of fit considering the large number of spectra being fit simultaneously. Generalized ellipsometry consists of three ratios for N , C , and S ; since data are measured at three azimuthal rotations, there are a total of 27 sets of data being fit simultaneously during the divided spectral range and numerical inversion steps for data collected from each crystal.

Numerically inverted spectra in ϵ_2 in each crystallographic direction are fitted simultaneously along with their first derivatives $d\epsilon_2/dE$ in critical point analysis using CPPB oscillators over a spectral range where the magnitude of ϵ_2 is >0.5 in order to omit sub gap absorption as shown in Fig. 1 and Table II along the a-axis, Table III along the c-axis, and Table IV along the b-axis. This approach yields greater sensitivity to critical point dimensionalities compared to fitting either ϵ_2 or $d\epsilon_2/dE$ only. Parameters used in the CPPB oscillators are coupled appropriately with the parameters used in the derivatives of the CPPB

oscillators. Every combination of dimensionalities is tested, and those yielding the highest quality of fit are used for the final parameterization. Critical points with ϕ_n that are equal to integer multiples of $\pi/2$, such as the critical points at 7.14 eV along the b-axis and 7.16 eV along the a-axis, represent transitions between noncorrelated one-electron bands.²¹ When the phases are non-integer multiples of $\pi/2$, as is the case for the critical points located at 6.50 and 7.21 eV along the b-axis and 7.42 eV along the c-axis, excitonic effects are involved. When the dimensionality is excitonic but the phase does not equal zero, which occurs at the critical points located at 6.99 eV along the a-axis and 7.21 eV along the b-axis, the discrete excitation may be interacting with continuous background absorption. Overall, the combinations of ϕ_n and μ_n indicate interactions with background effects and excitonic effects. The spectrum in ϵ_2 along the b-axis contains the lowest absorption onset at 6.5 eV, indicating that this is the direction featuring the optical bandgap. There is a sharp decrease in absorption below the transition energy, and the spectrum is adequately described using CPPB oscillators, indicating that the bandgap is direct. The onsets along the a- and c-axes occur at ~ 7 eV or higher, and feature more gradual absorption tails below the lowest critical points in those directions due to suppression in lower energy optical transitions between 6.5 and ~ 7.0 eV along these directions relative to that parallel to the b-axis.

Numerically inverted spectra in ϵ obtained over the full measured spectral range parallel to the b-axis, which contains the lowest energy transition of all three axes, are fit to parametric models consisting of critical point transitions represented by CPPB oscillators above the bandgap energy²³ and an exponentially decaying Urbach tail below the gap defined as²²

TABLE II. Critical point parabolic band (CPPB) parameters fitting to numerically inverted data along the a-axis while simultaneously fitting to the derivative of ϵ_2 .

Parameter, critical point $n =$	0	1
E_n (eV)	6.99 ± 0.09	7.16 ± 0.01
A_n	5.83 ± 2.62	13.97 ± 3.20
Γ_n (eV)	0.73 ± 0.19	0.43 ± 0.03
ϕ_n ($^\circ$)	-270 ± 25	0
μ_n	1	0.5

TABLE III. CPPB parameters fitting to numerically inverted data along the c-axis while simultaneously fitting to the derivative of ϵ_2 .

Parameter, critical point $n =$	0	1
E_n (eV)	7.21 ± 0.03	7.42 ± 0.46
A_n	8.64 ± 4.46	21.2 ± 14.6
Γ_n (eV)	0.171 ± 0.062	1.22 ± 0.74
ϕ_n ($^\circ$)	244 ± 21	64.0 ± 22.5
μ_n	-0.5	-0.5

TABLE IV. CPPB + Urbach parameters along the b-axis. Urbach energy is no more than 20 meV. The real part of ϵ is obtained from Kramers–Kronig integration and a Sellmeier expression with a resonance at 10.2 ± 0.3 eV and an amplitude of 28.1 ± 2.7 . The σ in fitting ϵ_1 is 8.26×10^{-3} , and the σ of ϵ_2 is 3.62×10^{-3} .

Parameter, critical point $n =$	0	1	2
E_n (eV)	6.50 ± 0.04	7.14 ± 0.02	7.21 ± 0.03
A_n	1.18 ± 0.39	21.4 ± 3.03	9.66 ± 2.35
Γ_n (eV)	0.142 ± 0.051	0.391 ± 0.046	0.451 ± 0.041
ϕ_n (°)	-59.1 ± 39.1	0	-178 ± 13
μ_n	0.5	0.5	1

$$\epsilon_2 = \begin{cases} \frac{E_0}{E} \exp\left[\frac{E - E_t}{E_U}\right], & 0 < E \leq E_t \\ \text{Im}[\epsilon_{\text{CPPB}}(E)], & E > E_t, \end{cases} \quad (4)$$

where $E_t = E_0 + 0.5E_U$ for a direct transition, E_0 is the lowest energy critical point transition, and the parameter E_U represents the Urbach tail width. This modification of the standard critical point parabolic band model retains physically realistic parameters, which allows for comparison of critical points obtained from spectra in ϵ and its derivatives as well as the Urbach energy which may be obtained from other measurements. Other parametric models such as Johs–Herzinger,^{24,25} B-splines,²⁶ Tauc–Lorentz,^{27,28} and non-KK consistent CPPBs²⁰ may have larger numbers of fit parameters or those without direct physical meaning to generate similar lineshapes of ϵ , which may increase the risk of errors and parameter correlations. Critical point parameters are already obtained by fitting ϵ_2 and $d\epsilon_2/dE$ simultaneously, leaving E_U as the only independent parameter describing ϵ_2 . However, the data do not have sensitivity to the Urbach energy due to the spectral resolution but show only that $E_U \leq 20$ meV to obtain qualitative agreement with the numerically inverted spectra in ϵ_2 . Spectra in ϵ_1 are obtained from Kramers–Kronig integration of the respective spectra in ϵ_2 .²²

$$\epsilon_1 = \epsilon_\infty + \frac{2}{\pi} \left(\frac{A_1 E_1}{E_1^2 - E^2} \right) + \frac{2}{\pi} P \int_{0.73}^{8.5} \frac{\xi \epsilon_2(\xi)}{\xi^2 - E^2} d\xi, \quad (5)$$

where ϵ_∞ is fixed at unity and P is the Cauchy principal part of the integral along with Sellmeier expression terms. The Sellmeier expression accounts for contributions to ϵ_1 arising from absorption features outside the range of the Kramers–Kronig integral. Parameter values along the b-axis are shown in Table III.

To parameterize ϵ along the a- and c-axes, the numerically inverted spectra are fitted to CPPB oscillators modified by a Cody band edge function (G_c),

$$\epsilon_2 = \begin{cases} 0, & 0 < E \leq E_g, \\ G_c(E) \text{Im}[\epsilon_{\text{CPPB}}(E)], & E > E_g, \end{cases} \quad (6)$$

where G_c is defined as

$$G_c(E) = \frac{(E - E_g)^2}{(E - E_g)^2 + E_p^2}, \quad (7)$$

TABLE V. CPPB with Cody band edge parameters fitting to numerically inverted spectra in ϵ parallel to the a-axis. Parameters not specified are fixed to values obtained by the critical point analysis in Table II. The error (σ) is 4.73×10^{-3} in fitting ϵ_1 and 3.05×10^{-3} for ϵ_2 .

Sellmeier energy (eV)	9.66 ± 0.11
Sellmeier amplitude (eV)	22.4 ± 1.1
ϵ_∞	1
A_1	10.4 ± 5.3
ϕ_1 (°)	-50.6 ± 14.4
A_2	25.4 ± 8.0
E_g (eV)	6.72 ± 0.06

where E_p represents the transition from band edge behavior to critical point behavior in ϵ_2 and is defined as the difference between an absorption onset energy, E_g , which lies between the direct gap at 6.50 eV identified in ϵ parallel to the b-axis and the lowest critical point energy in the a- or c-axis direction.²² In ϵ_2 parallel to the a- and c-axes, the lowest observed transition at 6.5 eV is suppressed relative to that along the b-axis, with absorption between 6.5 and ~ 7.0 eV due to the continuous background of band-to-band transitions. The parameters ϕ_1 , Γ_n , and μ_n are fixed to the values obtained by fitting ϵ_2 and $d\epsilon_2/dE$ simultaneously. A_0 and ϕ_0 are the only fit parameters needed, since the Cody band edge function only affects the critical point amplitudes and the region near the lowest critical point when compared to the CPPB parameterization alone. ϵ_1 is obtained from Kramers–Kronig integration, a Sellmeier expression, and ϵ_∞ . Parameters along the a- and c- axes are shown in Tables V and VI, respectively.

A comparison of the complex optical properties determined in the direction of each axis described by the parametric models using Eqs. (4)–(7) along with the numerically inverted data is shown in Fig. 2. The lowest critical point, due to a direct bandgap transition, lies in the b-axis and is found to be 6.50 ± 0.04 eV. There is a common critical point transition at 7.21 ± 0.03 eV in ϵ along both the b- and c-axes. A transition in ϵ along the a-axis at 7.16 ± 0.01 eV may be due to the same effect as that observed along the b-axis at 7.14 ± 0.02 eV. Additional critical points occur at 6.99 \pm 0.09 eV along the a-axis and 7.42 \pm 0.46 eV along the c-axis. The relatively high error in this final critical point energy along the c-axis may be due to high correlation with its amplitude and the relatively greater broadening of this feature with $\Gamma > 1.0$ eV compared to the other observed transitions.

TABLE VI. CPPB with Cody band edge parameters fitting to numerically inverted spectra in ϵ parallel to the c-axis. Parameters not specified are fixed to values obtained by the critical point analysis in Table III. The σ is 4.03×10^{-3} in fitting ϵ_1 and 2.85×10^{-3} for ϵ_2 .

Sellmeier energy (eV)	9.88 ± 0.12
Sellmeier amplitude (eV)	23.4 ± 10
ϵ_∞	1
A_1	282 ± 49
Φ_1 (°)	231 ± 6
A_2	64.0 ± 3.3
E_g (eV)	6.74 ± 0.04

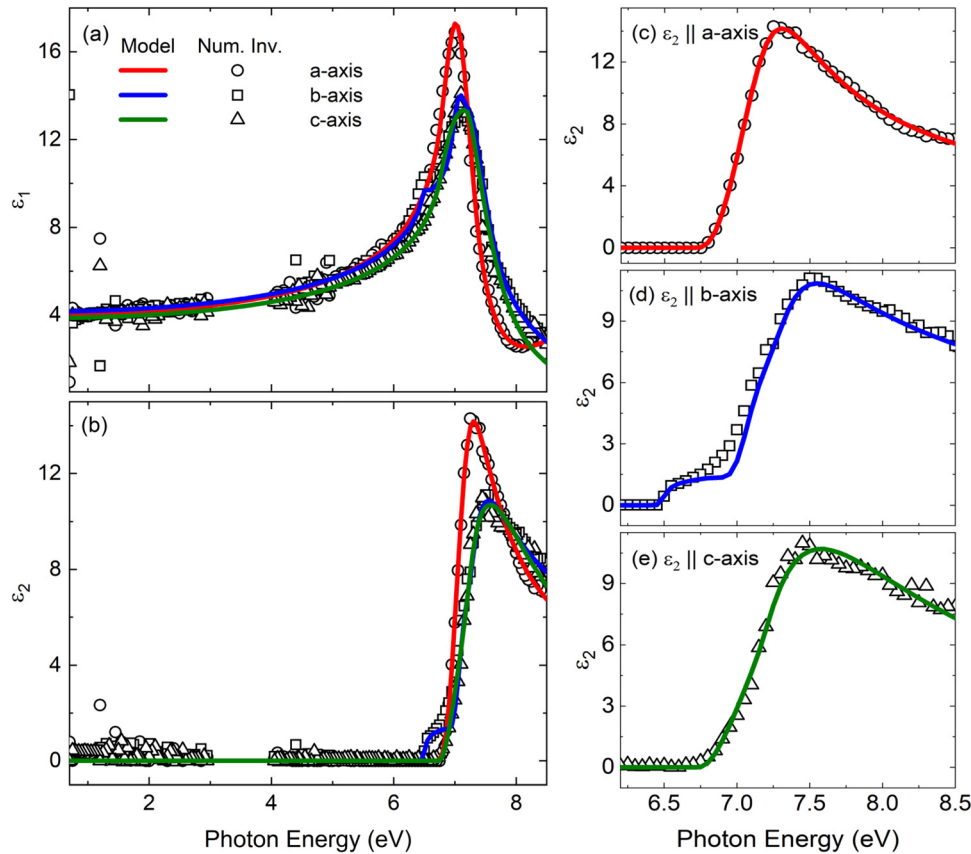


FIG. 2. (a) and (b) Spectra in ϵ of TbScO₃ obtained from numerical inversion (open symbols) and parameterization of ϵ (solid lines) along each direction from 0.7 to 8.5 eV. (c)–(e) Spectra in ϵ_2 along each axis in the vicinity of the bandgap and absorption onset from 6.2 to 8.5 eV.

Christen *et al.*⁵ report the bandgap of TbScO₃ as 5.41 eV obtained from spectroscopic ellipsometry for epitaxial thin film TbScO₃ deposited on a pseudocubic LaAlO₃ substrate, introducing strain to the crystal lattice. Cicerella also studied TbScO₃ deposited on LaAlO₃ and reports the bandgap as 5.6 eV as measured using a spectroscopic ellipsometry.⁶ Derks *et al.*⁷ characterize the Czochralski method grown single crystal TbScO₃ by x-ray absorption spectroscopy and x-ray emission spectroscopy, reporting the bandgap as 6.1 eV. These differences in bandgap energies may be partially attributed to strain in the case of epitaxial thin film material and to different methods of extracting the bandgap value compared to the critical point analysis reported here for single crystals. In experiments where the TbScO₃ is grown on a substrate, lattice mismatch may introduce strain into the TbScO₃, simultaneously affecting its lattice parameters, band structure, and bandgap energy.^{29,30}

The anisotropic optical properties for electric fields oscillating parallel to each crystallographic axis of single crystal TbScO₃ have been determined over a spectral range of 0.7–8.50 eV from analysis of generalized ellipsometric spectra. The direct optical bandgap has been identified as 6.50 ± 0.04 eV, slightly higher than previously reported values. Direct transitions in ϵ have been identified at 6.99 ± 0.09 eV along the a-axis, 7.14 ± 0.02 eV along the b-axis, 7.16 ± 0.01 eV along the a-axis, 7.21 ± 0.03 eV along the b- and c-axes, and 7.42 ± 0.46 eV

along the c-axis. Dimensionality and phase values indicate interactions of background and excitonic effects for each critical point.

See the supplementary material for more information and figures, such as ellipsometry data of TbScO₃ plotted with divided spectral range models and numerical inversion spectra, x-ray diffraction results, line shapes of the individual oscillators comprising the final parameterization of ϵ_2 , a schematic of the complete analysis procedure, and more.

This material is based on research sponsored by the Air Force Research Laboratory under Agreement Nos. FA9453-18-2-0037, FA9453-19-C-1002, and FA9453-21-C-0056. The U.S. Government is authorized to reproduce and distribute reprints for Governmental purposes notwithstanding any copyright notation thereon. The views expressed are those of the authors and do not reflect the official guidance or position of the United States Government, the Department of Defense, or of the United States Air Force. The appearance of external hyperlinks does not constitute endorsement by the United States Department of Defense (DoD) of the linked websites, or the information, products, or services contained therein. The DoD does not exercise any editorial, security, or other control over the information you may find at these locations.

Approved for public release; distribution is unlimited. The Public Affairs release Approval No. is AFRL-2022-2642.

AUTHOR DECLARATIONS

Conflict of Interest

The authors have no conflicts to disclose.

Author Contributions

Emily Amonette: Data curation (lead); Formal analysis (lead); Investigation (lead); Methodology (equal); Writing – original draft (lead); Writing – review & editing (lead). **Prabin Dulal:** Data curation (supporting). **Dylan Sotir:** Data curation (supporting); Formal analysis (supporting). **Matthew R. Barone:** Data curation (supporting); Formal analysis (supporting). **Darrell G. Schlom:** Supervision (supporting). **Nikolas Podraza:** Conceptualization (lead); Funding acquisition (lead); Methodology (lead); Supervision (lead); Writing – review & editing (supporting).

DATA AVAILABILITY

The data that support the findings of this study are available within the article and its supplementary material.

REFERENCES

- E. Cianci, A. Lamperti, G. Congedo, and S. Spiga, “Structural and electrical properties of terbium scandate films deposited by atomic layer deposition and high temperature annealing effects,” *ECS J. Solid State Sci. Technol.* **1**, P5 (2012).
- M. Roeckerath, J. M. J. Lopes, E. Durgun Ozben, C. Urban, J. Schubert, S. Mantyl, Y. Jia, and D. G. Schlom, “Investigation of terbium scandate as an alternative gate dielectric in fully depleted transistors,” *Appl. Phys. Lett.* **96**, 013513 (2010).
- M. Folkman, S. H. Baek, H. W. Jang, C. B. Eom, C. T. Nelson, X. Q. Pan, Y. L. Li, L. Q. Chen, A. Kumar, V. Gopalan, and S. K. Streiffner, “Stripe domain structure in epitaxial (001) BiFeO₃ thin films on orthorhombic TbScO₃ substrate,” *Appl. Phys. Lett.* **94**, 251911 (2009).
- B. Veličkov, V. Kahlenberg, R. Bertram, and R. Uecker, “Redetermination of terbium scandate, revealing a defect-type perovskite derivative,” *Acta Crystallogr.* **E64**, i79 (2008).
- H. M. Christen, G. E. Jellison, Jr., I. Ohkubo, S. Huang, M. E. Reeves, E. Cicerrella, J. L. Freeouf, Y. Jia, and D. G. Schlom, “Dielectric and optical properties of epitaxial rare-earth scandate films and their crystallization behavior,” *Appl. Phys. Lett.* **88**, 262906 (2006).
- E. Cicerrella, “Dielectric functions and optical bandgaps of high-K dielectrics by far ultraviolet spectroscopic ellipsometry,” Ph.D. dissertation (Oregon Health and Science University, 2006).
- C. Derks, K. Kuepper, M. Raekers, A. V. Postnikov, R. Uecker, W. L. Yang, and M. Neumann, “Band-gap variation in RScO₃ (R=Pr, Nd, Sm, Eu, Gd, Tb, and Dy): X-ray absorption and O K-edge x-ray emission spectroscopies,” *Phys. Rev. B* **86**, 155124 (2012).
- L. Karki Gautam, H. Haneef, M. M. Junda, D. B. Saint John, and N. J. Podraza, “Approach for extracting complex dielectric function spectra in weakly-absorbing regions,” *Thin Solid Films* **571**, 548–553 (2014).
- H. F. Haneef and N. J. Podraza, “Optical properties of single crystal Bi₄Ge₃O₁₂ from the infrared to ultraviolet,” *J. Appl. Phys.* **116**, 163507 (2014).
- K. Ghimire, H. Haneef, R. W. Collins, and N. J. Podraza, “Optical properties of single-crystal Gd₃Ga₅O₁₂ from the infrared to ultraviolet,” *Phys. Status Solidi B* **252**(10), 2191–2198 (2015).
- T. Wagner, J. N. Hilfiker, T. E. Tiwald, C. L. Bungay, and S. Zollner, “Materials characterization in the vacuum ultraviolet with variable angle spectroscopic ellipsometry,” *Phys. Status Solidi A* **188**, 1553–1562 (2001).
- G. E. Jellison and J. S. Baba, “Pseudodielectric functions of uniaxial materials in certain symmetry directions,” *J. Opt. Soc. Am. A* **23**, 468–475 (2006).
- B. Johs and C. M. Herzinger, “Quantifying the accuracy of ellipsometer systems,” *Phys. Status Solidi C* **5**, 1031 (2008).
- S. A. Alterovitz and B. Johs, “Multiple minima in the ellipsometric error function,” *Thin Solid Films* **313–314**, 124 (1998).
- CompleteEASE Software Manual. J.A. Woollam Co., Lincoln, NE, 2004–2014. p. 240.
- W. G. Oldham, “Numerical techniques for the analysis of lossy films,” *Surf. Sci.* **16**, 97 (1969).
- H. Fujiwara, J. Koh, P. I. Rovira, and R. W. Collins, “Assessment of effective-medium theories in the analysis of nucleation and microscopic surface roughness evolution for semiconductor thin films,” *Phys. Rev. B* **61**, 10832 (2000).
- R. W. Collins and H. Fujiwara, “Growth of hydrogenated amorphous silicon and its alloys,” *Curr. Opin. Solid State Mater. Sci.* **2**, 417–424 (1997).
- R. W. Collins and A. S. Ferlauto, in *Handbook of Ellipsometry*, edited by H. G. Tompkins and E. A. Irene (William Andrew, Norwich, NY, 2005), pp. 92–235.
- D. E. Aspnes, in *Handbook of Semiconductors*, edited by M. Balkanski (North-Holland Publishing Company, Amsterdam, 1980), Vol. 2, pp. 125–127.
- P. Lautenschlager, M. Garriga, S. Logothetidis, and M. Cardona, “Interband critical points of GaAs and their temperature dependence,” *Phys. Rev. B* **35**, 9174–9189 (1987).
- A. S. Ferlauto, G. M. Ferreira, J. M. Pearce, C. R. Wronski, and R. W. Collins, “Analytical model for the optical functions of amorphous semiconductors from the near-infrared to ultraviolet: Applications in thin film photovoltaics,” *J. Appl. Phys.* **92**, 2424 (2002).
- S. Loughin, R. H. French, L. K. De Noyer, W. Y. Ching, and Y. N. Xu, “Critical point analysis of the interband transition strength of electrons,” *J. Phys. D: Appl. Phys.* **29**, 1740–1750 (1996).
- B. Johs, C. M. Herzinger, J. H. Dinan, A. Cornfeld, and J. D. Benson, “Development of a parametric optical constant model for Hg_{1-x}Cd_xTe for control of composition by spectroscopic ellipsometry during MBE growth,” *Thin Solid Films* **313–314**, 137–142 (1998).
- C. M. Herzinger, B. Johs, W. A. McGahan, J. A. Woollam, and W. Paulson, “Ellipsometric determination of optical constants for silicon and thermally grown silicon dioxide via a multi-sample, multi-wavelength, multi-angle investigation,” *J. Appl. Phys.* **83**, 3323 (1998).
- B. Johs and J. S. Hale, “Dielectric function representation by B-splines,” *Phys. Status Solidi A* **205**, 715–719 (2008).
- G. E. Jellison, Jr. and F. A. Modine, “Parameterization of the optical functions of amorphous materials in the interband region,” *Appl. Phys. Lett.* **69**, 371 (1996).
- A. Tejada, S. Peters, A. Al-Ashouri, S. H. Turren-Cruz, A. Abate, S. Albrecht, F. Ruske, B. Rech, J. A. Guerra, and L. Korte, “Hybrid perovskite degradation from an optical perspective: a spectroscopic ellipsometry study from the deep ultraviolet to the middle infrared,” *Adv. Opt. Mater.* **10**(3), 2101553 (2022).
- C. P. Kuo, S. K. Vong, R. M. Cohen, and G. B. Stringfellow, “Effect of mismatch strain on band gap in III-V semiconductors,” *J. Appl. Phys.* **57**, 5428 (1985).
- L. Huang, Z. Chen, and J. Li, “Effects of strain on the band gap and effective mass in two-dimensional monolayer GaX (X=S, Se, Te),” *RSC Adv.* **5**, 5788–5794 (2015).
- G. E. Jellison, N. J. Podraza, and A. Shan, “Ellipsometry: Dielectric functions of anisotropic crystals and symmetry,” *J. Opt. Soc. Am. A* **39**(12), 2225–2237 (2022).

Supplementary Information for Band Gap Energy and Near Infrared to Ultraviolet

Complex Optical Properties of Single Crystal TbScO₃

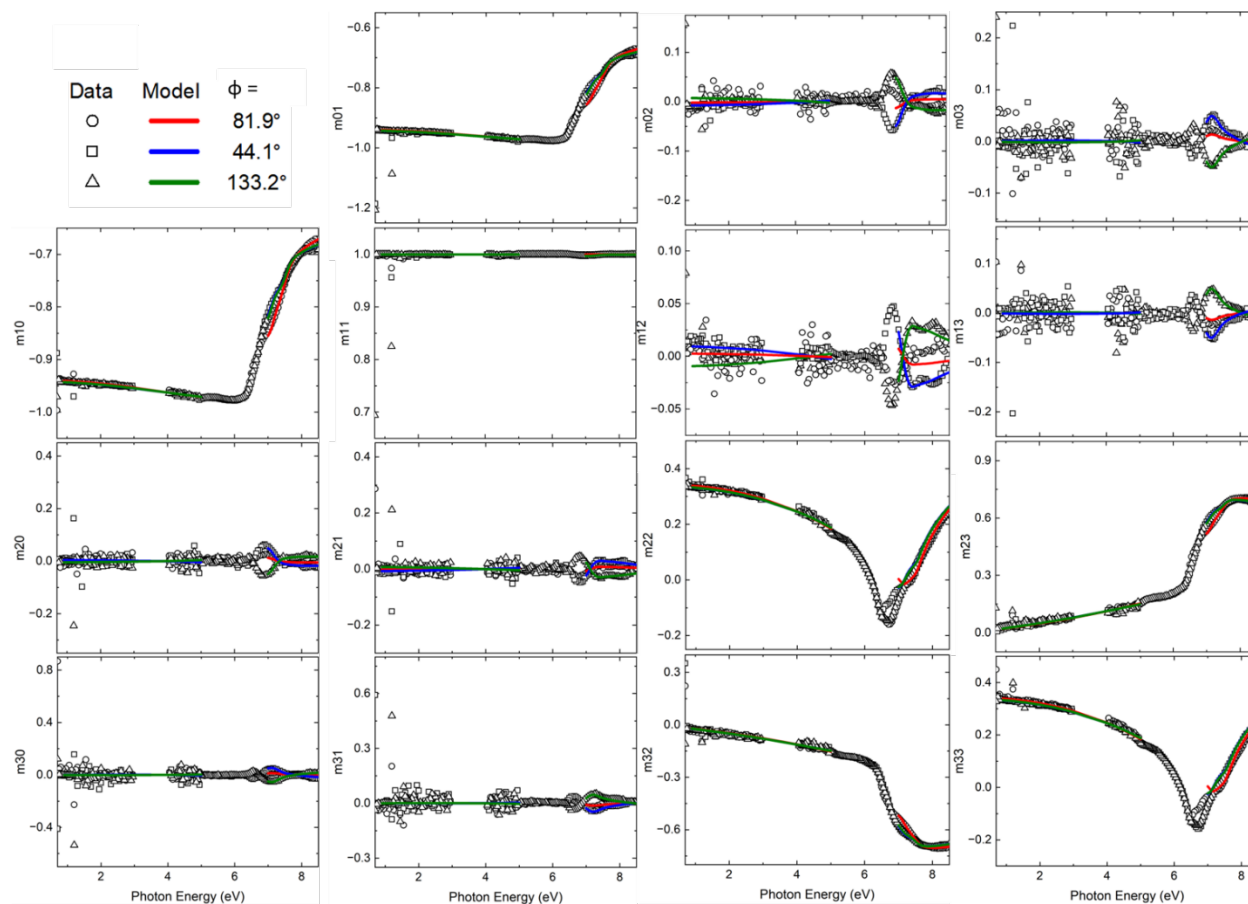


Figure S-1 Mueller matrix spectra (open symbols) and parameterized models (solid lines) obtained using divided spectral range analysis on a (001) TbScO₃ single crystalline sample. Generalized ellipsometry spectra have been converted to Mueller matrix spectra assuming no depolarization as per Jellison et al. [31] for display purposes. The error (σ) is 7.92×10^{-2} . This σ is acceptable considering the large number of data sets being fit simultaneously.

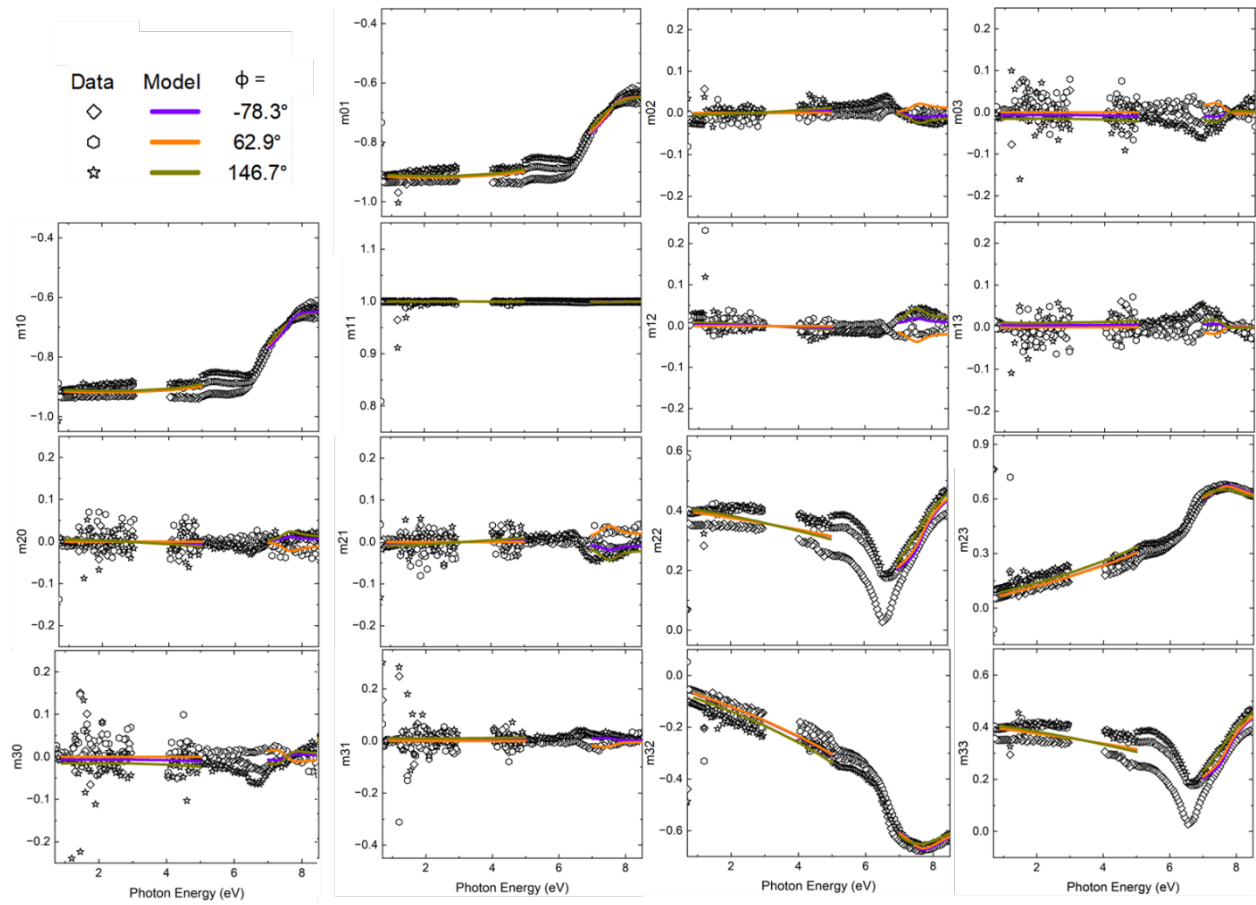


Figure S-2 Mueller matrix spectra (open symbols) and parameterized models (solid lines) obtained using divided spectral range analysis on a (110) TbScO₃ single crystalline sample. Generalized ellipsometry spectra have been converted to Mueller matrix spectra assuming no depolarization as per Jellison et al. [31] for display purposes. The σ is 6.87×10^{-2} . This σ is acceptable considering the large number of data sets being fit simultaneously.

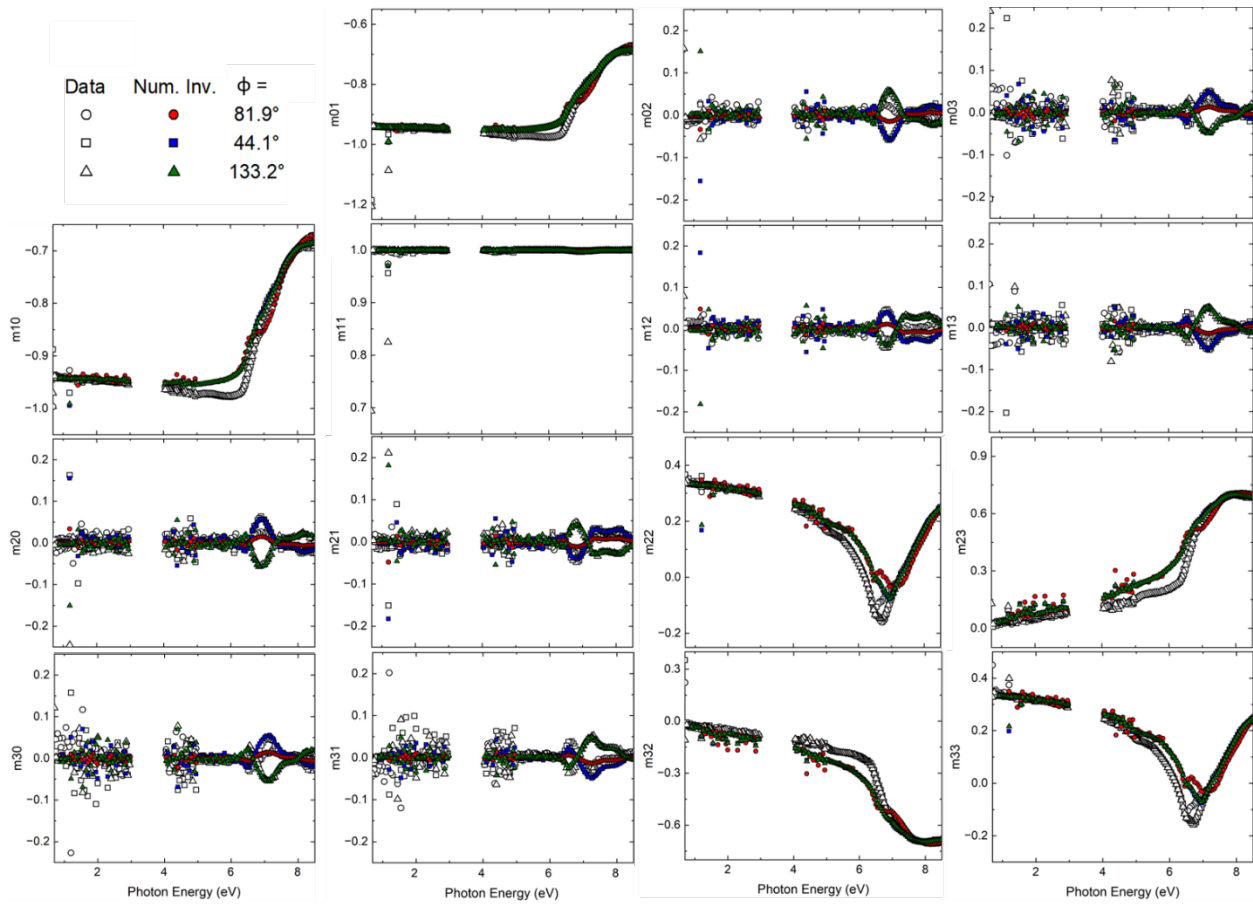


Figure S-3 Mueller matrix spectra (open symbols) and numerical inversion spectra (solid symbols) of a (001) TbScO₃ single crystalline sample. The σ is 6.45×10^{-2} .

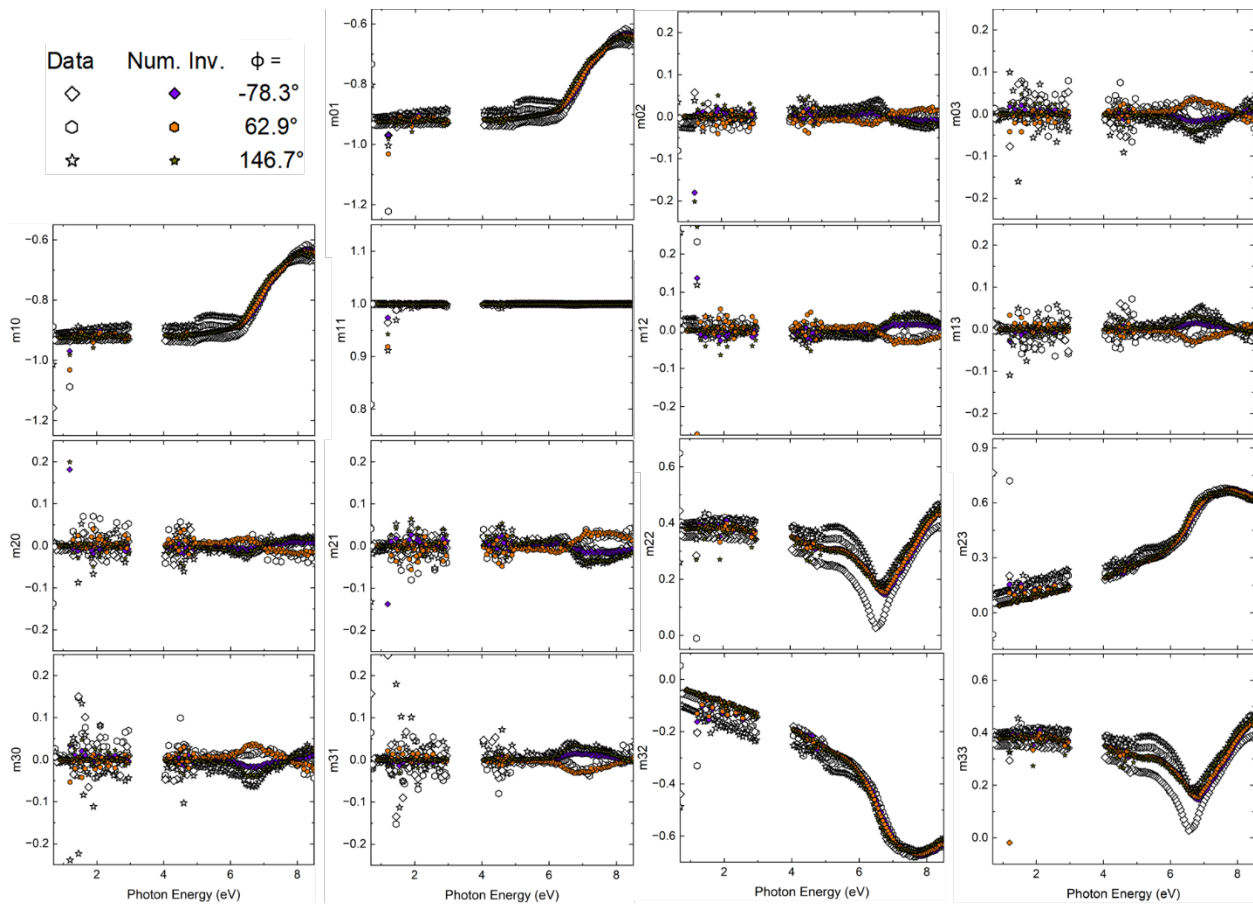


Figure S-4 Mueller matrix spectra (open symbols) and numerical inversion spectra (solid symbols) of a (110) TbScO₃ single crystalline sample. The σ is 6.43×10^{-2} .

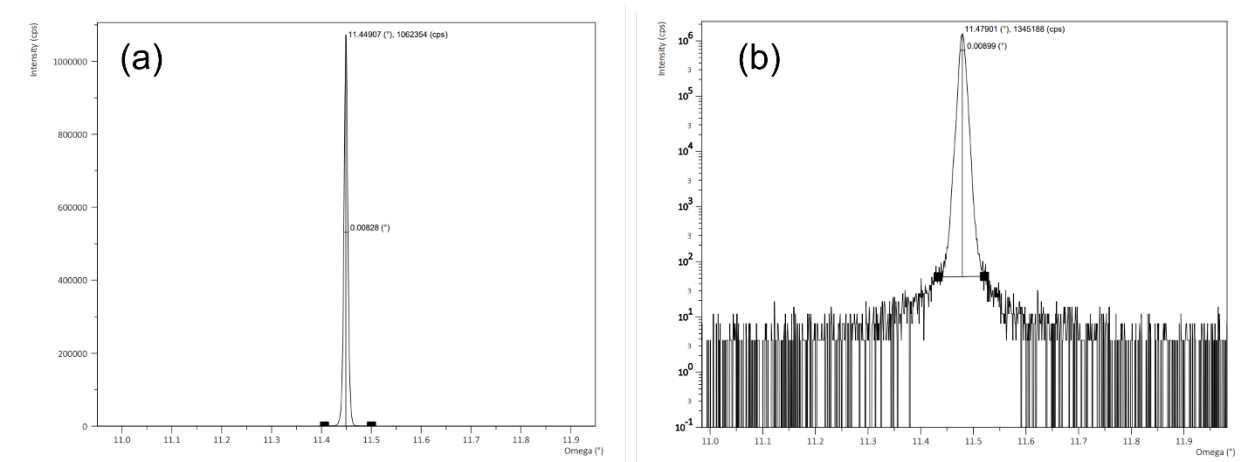


Figure S-5 Rocking curve x-ray diffraction scans for (a) a (110) surface plane oriented TbScO₃ single crystal with a full width half maximum peak of 0.00828° and (b) a (001) surface plane oriented single crystal with a full width half maximum peak of 0.00899°.

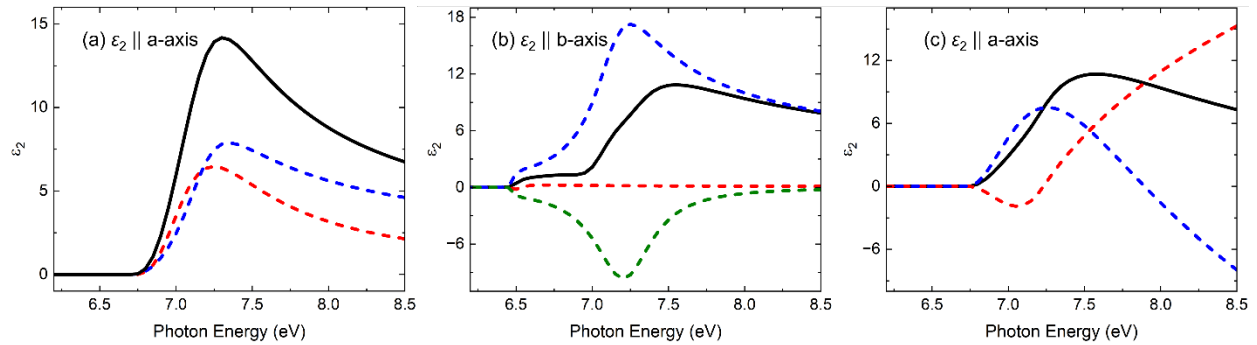


Figure S-6 Decomposition of spectra in ϵ_2 (solid lines) into individual CPPB oscillator contributions (dashed lines) for electric fields oscillating parallel to the a-, b-, and c-axes.

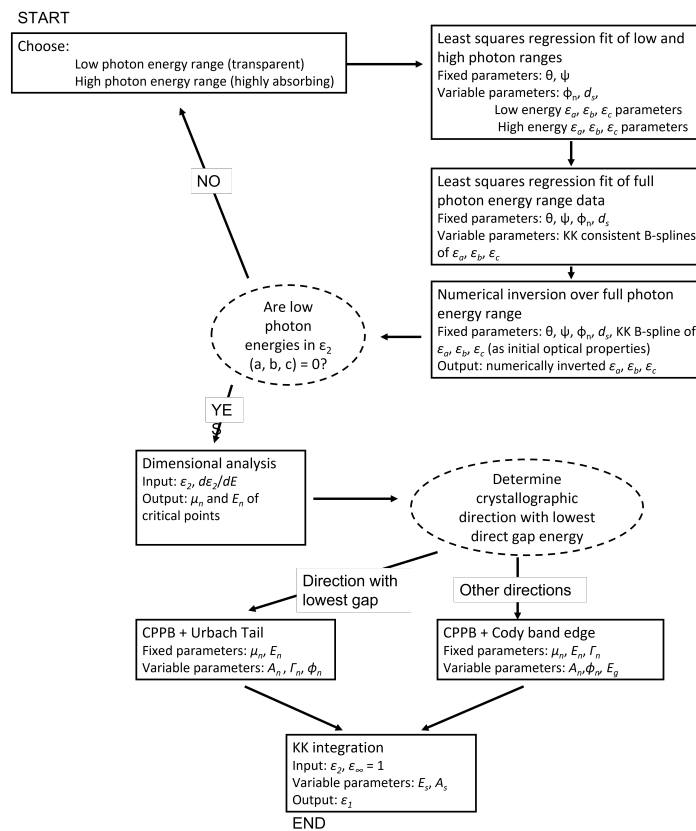


Figure S-7 Flow chart of the divided spectral range analysis technique used in this work, where θ , Ψ , and ϕ_n are Euler angles, d_s is the surface layer thickness, μ_n , E_n , A_n , Γ_n , and ϕ_n are the dimensionality, critical point energy, amplitude, broadening, and phase of a CPPB oscillator, E_g is the absorption onset energy of the Cody band edge function, and E_s and A_s are the energy and amplitude of a Sellmeier function.